ADVANCED ENGINEERING MATERIALS
www.aem-journal.com

Deformation Behavior and Fracture Strength of Single-Crystal 4H-SiC Determined by Microcantilever Bending Tests

Tsukaho Yahagi, Tatsuki Ohji, Hiroshi Yamaguchi, Takuma Takahashi, Hiromi Nakano, Motoyuki Iijima, and Junichi Tatami*

Dedicated to Professor Nahum Travitzky

In this study, the deformation behaviors and mechanical properties of 4H-SiC single crystals are investigated using microcantilever beam specimens with two different sizes, *A* and *B* (*A* < *B*). Tensile stress is applied along <$\bar{1}\,\bar{1}20$> direction. Plastic deformation, or nonlinearity, is observed in the stress–strain curves, and yield stress, or proportional limit, coincides between the two specimens at ≈25 ± 2 GPa. Scanning transmission electron microscopy and transmission electron microscopy studies show that the plastic deformation is due to dislocation activities; multiple-dislocation pileup areas are observed in both the specimens. Assuming {$1\bar{1}00$}/<$11\bar{2}0$> prismatic slip which most plausibly occurs in the <$\bar{1}\,\bar{1}20$> stress application, the critical resolved shar stress is estimated to be 10.9 GPa, which agrees well with the previous studies. Measured fracture strength is 41.9 ± 2.8 and 33.5 ± 2.4 GPa for the *A* and *B*, respectively. Dislocation–fracture relationship is discussed on the basis of dislocation-based fracture mechanics, etc. It is suggested that cracks form within the multiple-dislocation pileup area, by interaction with dislocation pileups, and act as fracture origins. *A*'s strength is close to an ideal tensile strength of 4H-SiC in the <$11\bar{2}0$> direction, 47–55 GPa.

1. Introduction

Silicon carbide (SiC) is widely used for a variety of engineering applications requiring high endurance, including structural components,[1] abrasive parts,[2] automobile parts,[3,4] filters and porous membranes,[5,6] combustion reactors,[7,8] light-emitting diodes (LEDs) and microwave devices,[9] space mirrors and optical devices,[10] and power electronic devices.[11,12] In particular, SiC semiconductors have been studied extensively for power devices, since they are operatable at higher voltage, higher switching frequency, and higher temperatures than silicon. SiC has a large number of polytypes, including cubic 3C-SiC, hexagonal 4H- and 6H-SiC, and rhombohedral 15R-SiC.[13] Among these polytypes, 4H-SiC has attracted a lot of attention for the power device applications, because of its excellent properties of wide bandgap, high carrier mobility, high electric breakdown field, and high thermal conductivity.[11,12]

SiC is a hard chemical compound comprising covalently bonded silicon and carbon atoms and had been thought to be plastically deformable by dislocation glide only at high temperatures under uniaxial loading conditions. Recently, however, several studies using micropillar compression methods have revealed room-temperature plastic deformation behavior of SiC single crystals by dislocation glide. Shin et al.[14] performed room-temperature uniaxial compression tests for 3C-SiC using micropillars and found that ductile plasticity occurred in those of 0.65 μm diameter due to slip on {111} planes. The critical resolved shear stress (CRSS) was estimated to be 4.9–7.3 GPa

T. Yahagi, T. Ohji, H. Yamaguchi, T. Takahashi, M. Iijima, J. Tatami
Yokohama National University
79-5 Tokiwadai, Hodogayaku, Yokohama, Kanagawa 240-8501, Japan
E-mail: t-ohji@aist.go.jp

The ORCID identification number(s) for the author(s) of this article can be found under https://doi.org/10.1002/adem.202400095.

DOI: 10.1002/adem.202400095

T. Yahagi, T. Takahashi
Kanagawa Institute of Industrial Science and Technology
705-1 Shimoimaizumi, Ebina, Kanagawa 243-0435, Japan

T. Ohji
National Institute of Advanced Industrial Science and Technology (AIST)
Sakurazaka 4-205, Moriyama-ku, Nagoya, Aichi 463-8560, Japan

H. Nakano
Toyohashi University of Technology
1-1 Hibarigaoka, Tempaku-cho, Toyohashi, Aichi 441-8580, Japan

for {111}<110> slip systems. Kiani et al.[15] reported dislocation glide-controlled room-temperature plasticity in uniaxial compression of micropillars with sub-300 nm diameter of 6H-SiC single crystals; plastic slip occurred on (0001) basal planes along $<1\bar{1}00>$ directions at stresses above 7.8 GPa. Chen et al.[16] studied uniaxial compression behavior of 4H SiC nanopillars with a diameter of ≈180 nm at room temperature and revealed phase transformation from 4H structure to 3C one due to slip on (0001) basal planes along $<1\bar{1}00>$ directions at CRSS of 9–10 GPa. Kwon et al.[17] also observed room-temperature plastic deformation in uniaxial compression of micropillars with diameters below 0.49 μm for 6H-SiC single crystals. Clear slip traces and dislocations were identified on (0001) basal planes and the CRSS was determined to be 9.8 GPa. More recently, Kishida et al.[18] investigated room-temperature plastic deformation behavior of 6H-SiC single crystals by uniaxial compression of micropillar specimens with a square cross section having an edge length ranging from 1 to 7 μm and an aspect ratio of about 1:3. The (0001) basal and $\{1\bar{1}00\}$ prism slips were observed at CRSS values above 5 and 6 GPa, respectively, each of which increased with decreasing the specimen size and reached about 7 and 9 GP, respectively, at 1 μm edge length. It should be noted almost all of these studies indicated that plastic flow was not in bulk single crystals or single-crystal micropillars larger than certain sizes, most likely because of higher density of structural defects. In contrast, using first-principles calculations, Pizzagalli[19] theoretically estimated Peierls stresses for basal-plane slip systems in 2H-, 4H-, and 3C-SiC single crystals to be 9.6, 9.5, and 8.9 GPa, respectively.

It has been well known that dislocation activation and crack formation are heavily related with each other, and that dislocation pileups result in stress concentration and/or crack formation, leading to the final failure.[20–22] Therefore, it is critically important to correctly understand the linkage between dislocation and fracture behaviors. The previously stated micropillars studies on SiC single crystals were performed in compression, while fracture of materials normally occurs when a crack develops under tensile stress. Thus, the evaluation of the dislocation and fracture behaviors in tension is crucial for ensuring the reliability. Microcantilever method is an effective approach for this purpose, since it can measure the mechanical properties at microscopic scale under tensile stress. A load is applied at the tip of a microcantilever beam specimen to generate the bending stress on the specimen top surface until the failure occurs. Microscale mechanical properties have been investigated for various ceramic materials using this technique, and the effects of focused ion beam (FIB) milling, crystallographic orientation and microstructure on the properties have been reported.[23–34]

In this study, we evaluate deformation behaviors and mechanical properties of 4H-SiC single crystals using microcantilever beam specimens with two different sizes. Focusing on slip behaviors on planes excluding (0001) basal ones, tensile stress is applied along $<\bar{1}\,\bar{1}20>$ direction. The specimens were plastically deformed before failure, and the deformation and fracture behaviors are discussed in association with dislocation activities and crack formation.

2. Experimental Section

2.1. Specimen Preparation

Commercially available single crystals of 4H-SiC (ePAK International, Inc.) with the dimensions of $10 \times 15 \times 0.33$ mm were used in this study. Microcantilever beam specimens were fabricated by FIB combined with scanning electron microscopy (SEM) at FIB acceleration voltage of 30 kV (XVision 200TB, Hitachi High-Tech Corporation, Japan). A thin carbon coating was applied to the surfaces before machining to avoid machining damages. Two types of specimens were prepared, *A* and *B*, with different sizes as shown in **Table 1**. **Figure 1**a,b shows the side and front views of the specimen *B*, for example, as well as schematic illustration of *A* and *B* (Figure 1c). The top, side, and front surfaces were (0001), $(1\bar{1}00)$, and $(11\bar{2}0)$ planes, respectively, and the tensile stress was applied along $<\bar{1}\,\bar{1}20>$ direction. Their section profile was pentagonal because the bottom two planes were easily machinable from above by FIB processing. The sectional shape and sizes of each specimen were determined precisely for rigorous calculation of the second moment of area.

Table 1. Specimen sizes for microcantilever beam specimens *A* and *B*.

Specimen	*A*	*B*
Specimen sizes		
Width [μm]	0.5 ± 0.1	1.4 ± 0.2
Thickness [μm]	0.8 ± 0.1	1.5 ± 0.2
Length [μm]	4.6 ± 0.1	13.7 ± 1.5
Loading point-beam end distance [μm]	3.4 ± 0.1	9.5 ± 0.8

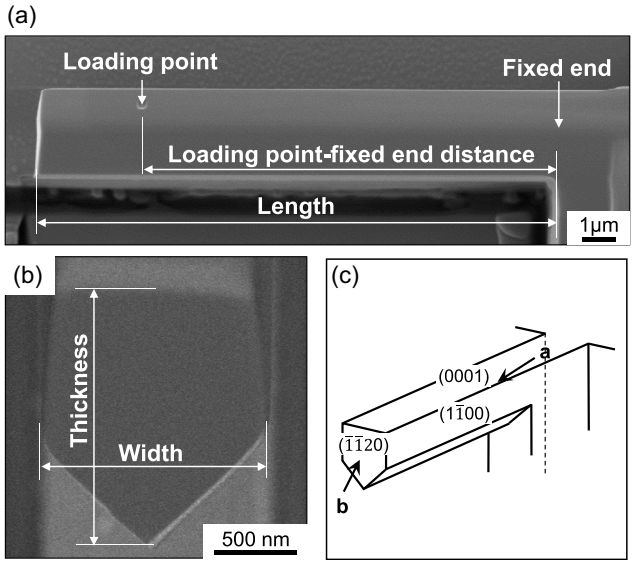

Figure 1. a) Side and b) front views of the specimen *B*. c) Schematic illustration of the specimens *A* and *B*. The top, side, and front surfaces are (0001), $(1\bar{1}00)$, and $(\bar{1}\,\bar{1}\,20)$ planes, respectively, and the tensile stress is applied along $<\bar{1}\,\bar{1}20>$ direction.

2.2. Microcantilever Bending Tests

The testing was performed by applying a load at the tip of a microcantilever beam specimen with a nanoindentation technique (TI Premier; Bruker Corporation, USA). The load was applied using a cube corner type diamond indenter at a displacement rate of 15 nm s^{-1} for the specimen *A* and 30 nm s^{-1} for *B*. Three specimens were used for each condition. The cube corner was advantageous to precisely placing the tip of the indenter at the loading point, which was beforehand marked on the centerline by an FIB technique (see Figure 1), enabling a correct loading.

The measured displacements of indentations generated during the microcantilever bending tests included both the depth of the indent itself and the displacement of the beam specimen at the loading point. Therefore, as shown in **Figure 2**, the load-indent depth curve (indentation curve) was separately determined by performing a general indentation test on a surface of the same single crystal using the same cube corner type diamond indenter as the bending test, and then the corrected curve was obtained by subtracting it from the measured. Some of the specimens were unloaded before fractures occurred to verify occurrence of plastic deformation. The stress and strain were calculated from the load and displacement using the following equations of beam theory:

$$\sigma = \frac{PLa}{I} \tag{1}$$

$$\varepsilon = \frac{3da}{L^2} \tag{2}$$

$$E = \frac{PL^3}{3dI} \tag{3}$$

where σ *is* the maximum bending stress (hereafter, bending stress), ε is the strain, E is Young's modulus, P is the applied load, L is the distance from the loading point to the fixed end (as shown in Figure 1), a is the distance between the top surface and the neutral plane, I is the cross-sectional secondary moment, and d is the displacement at the loading point. The cross-sectional secondary moment I was calculated considering the pentagonal shape and sizes. The detailed procedure for determining I is described in Supporting Information. The bending strength (or fracture strength) and yield stress were determined from the maximum load and the load at the proportional limit of the curve, respectively, using Equation (1).

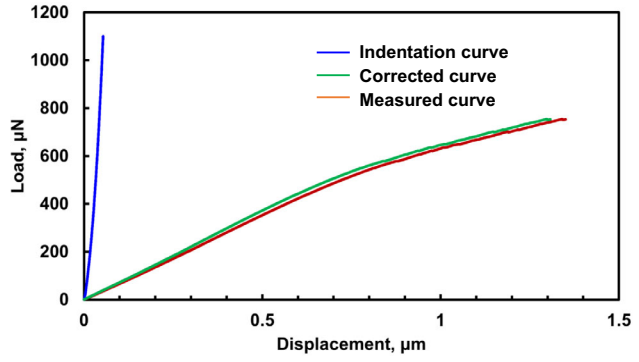

Figure 2. Corrected load–displacement curve obtained by subtracting indentation curve from measured one.

Muramoto et al.[33] (Supporting Information) conducted finite-element analyses for this type of microcantilever beam specimen and revealed that that both the maximum normal stress and the loading-point displacement linearly increased with increasing the applied load. However, the state of the stress distribution was not exactly homogeneous, and the maximum normal stress, which arose not precisely at the fixed end but slightly away (≈0.5 μm for 10 μm *L*) to the free end, was ≈6% lower than that of the beam theory.

Transmission electron microscopy (TEM) samples with a thickness of less than 100 nm were prepared using FIB–SEM (Scios; Thermo Fisher Scientific, Inc., USA) for pristine specimens (hereafter, reference) and specimens which were loaded and unloaded before fracture. The locations where TEM samples were extracted will be shown later. The acceleration voltage was set for 30 and 2 kV for the sample preparation and the final milling, respectively. The samples were observed using a TEM (Talos; Thermo Fisher Scientific, Inc., USA) at an acceleration voltage of 200 kV. Some transmission images were also obtained by scanning TEM (STEM). High-resolution TEM simulation image was constructed by ReciPro.[35]

3. Results and Discussion

3.1. Stress–Strain Curves

In the measured load–displacement curves, all the pieces of the specimens *A* and *B* indicated that the load linearly increased with increasing the displacement in the initial stage and then began to deviate from the linearity at a certain load. **Figure 3**a,b shows the stress–strain curves for *A* and *B*, respectively, which were calculated from the load–displacement curves using Equation (1) and (2). All the fractures occurred in the nonlinearity range. It should be noted that the stress and strain calculated based on the beam theory lack entire rigorousness.

The curves are very reproducible in the initial linear regions, and the Young's moduli calculated for these regions are listed in **Table 2**. Both the specimens *A* and *B* show the same value, 483 GPa, which is identical with that measured by an ultrasonic pulse method for 4H-SiC single crystals in $<\bar{1}\,\bar{1}20>$ direction.[36]

For the purpose of examining the observed nonlinear deformations, tests were conducted in which the specimens were unloaded after the nonlinearity, but before fracture, for both *A* and *B*. The obtained stress–strain curve for *B* is shown as an example in **Figure 4**. For both *A* and *B*, the loading and unloading curves did not coincide, demonstrating the permanent strain in the unloaded specimen after the nonlinearity appearance. This indicates that the 4H-SiC single crystals are plastically deformed under bending stress even at room temperature. The stress at the proportional limit is defined as a yield stress in this study and was determined using a procedure similar to that previously reported.[33] The yield stresses obtained for the specimens *A* and *B* are listed in Table 2, exhibiting that the two values coincide.

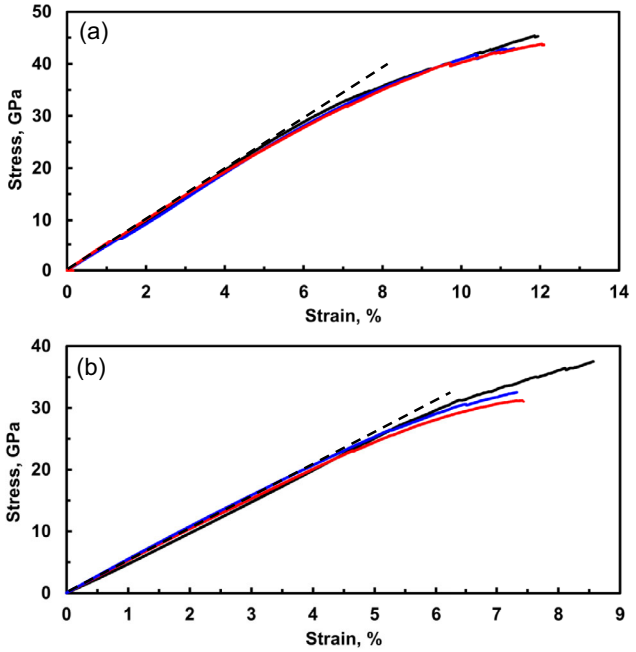

Figure 3. a,b) Stress–strain curves calculated from the load–displacement curves of the specimens *A* and *B*, respectively, using Equation (1) and (2). All the fractures occurred in the nonlinearity range.

Table 2. Mechanical properties, microscopic observations, and equivalent crack sizes for microcantilever beam specimens *A* and *B*.

Specimen	*A*	*B*
Mechanical properties		
Young's modulus, *E* [GPa]	483.8 ± 0.7	483.9 ± 1.6
Fracture strength, σ_f, [GPa]	41.9 ± 2.8	33.5 ± 2.4
Yield stress, σ_Y, [GPa]	25.1 ± 1.9	25.2 ± 1.6
CRSS (Equation (5)), τ_{CRSS} [GPa]	10.9	10.9
Microscopic observations		
Depth of defect area [nm]	15	150
Depth of multiple-dislocation pileup area [nm]	5–10	6–20
Depth of area subjected to yield stress or higher, *D* (Equation (4)) [nm]	107	181
Equivalent crack size, 2*c* (Equation (6))		
Griffith crack ($Y = 1$) [nm]	1.2	1.8
Penny-shaped crack ($Y = 2/\pi$) [nm]	2.9	4.5

3.2. STEM and TEM Observations

To investigate the sources causing the plastic deformation, STEM and TEM observations were performed for the specimens which had been loaded and unloaded before fracture. In the loading, the bending stress increased up to 37.1 and 32.1 GPa for the specimens *A* and *B*, respectively. **Figure 5**a,b shows STEM images of the unloaded specimens observed from [1$\bar{1}$00] direction for *A*

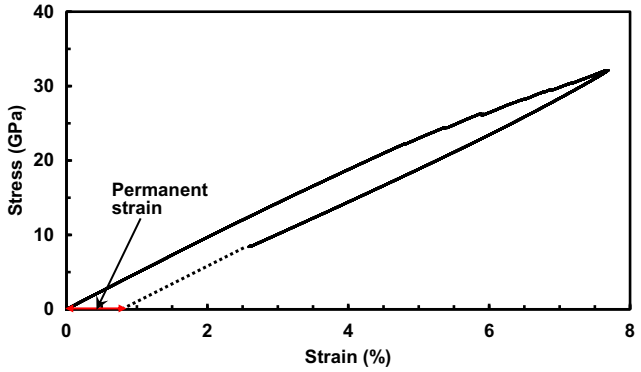

Figure 4. Stress–strain curves in the loading and unloading tests for the specimen *B*.

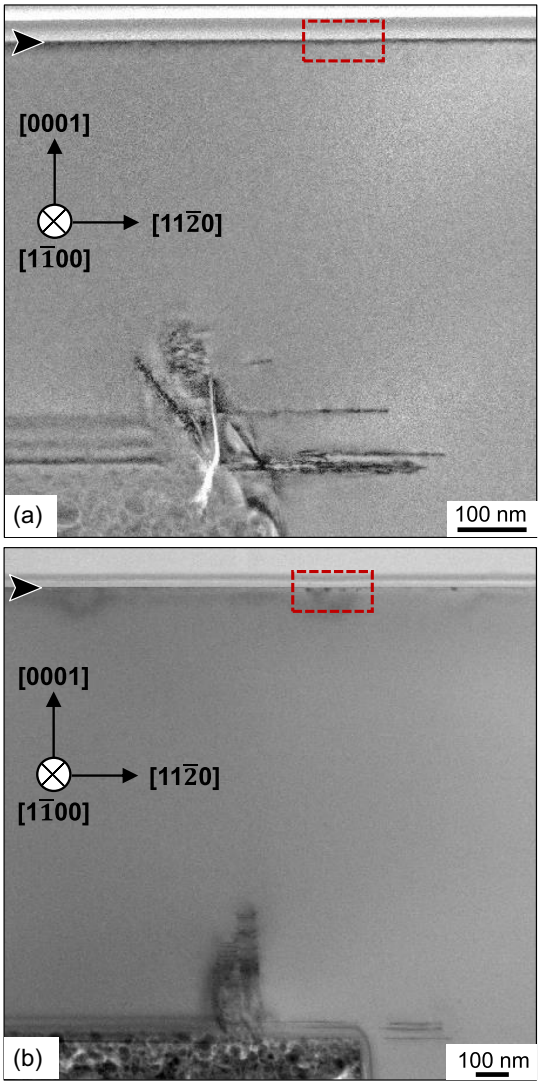

Figure 5. a,b) STEM images of the unloaded specimens observed from [1$\bar{1}$00] direction for the specimens *A* and *B*, respectively. ➤ indicates the surface of the specimen.

and *B*, respectively. The observation area is the beam base portion which was subjected to the maximum bending stress. Defects were identified in the vicinities of the top and bottom of the base. **Figure 6**a,b shows the magnified views of the top parts indicated by the red frames in Figure 5a,b, respectively. For comparison, an image from the same crystal direction $[1\bar{1}00]$ for the reference (non-loaded) is also given in Figure 6c. The dark dense area of defects is seen in Figure 6a,b, and the depth of the area is ≈15 and 150 nm, respectively (Table 2). Because of the lower stress gradient, the horizontal border of the area was not clearly discernible in either of the two specimens. On the contrary, such dark areas are not observed in the reference (Figure 6c). While there is a possibility that the crystal structure of 4H-SiC is damaged by Ga ions during the FIB process, the image with little disorder (Figure 6c) indicates that the influence of Ga ions is negligible.

It is possible to estimate the depth of the area which was subjected to a tensile stress higher than the yield stress, σ_Y, by using the following equation.

$$D = \frac{(\sigma_D - \sigma_Y)a}{\sigma_D} \quad (4)$$

where σ_D is the bending stress applied in the loading, being 37.1 and 32.1 GPa for *A* and *B*, respectively. The top surface-neutral plane distance, *a*, is 0.332 and 0.845 μm for *A* and *B*, respectively. The calculated *D* is 107 nm for *A* and 181 nm for *B* (Table 2). Comparing them with the defect area depth (15 and 150 nm, respectively), one can see a relatively good agreement for *B* but some discrepancy for *A*. The latter is most likely due to defect formation which is invisible in the STEM observation. The defect area depth, 15 nm, for *A* is the depth of the dark area observed in Figure 6a; it does not mean that dislocations are not generated below the dark area, and it can be presumed that the detailed TEM studies would detect the evidence of dislocations there.

Figure 7a,b shows TEM images of the areas of heavily disordered crystal structures with multiple-dislocation pileups observed in Figure 6a,b, respectively. It is found that the depth of the multiple-dislocation pileups area is 5–10 nm for the specimen *A* and 6–20 nm for *B* (Table 2). This difference between *A* and *B* can be explained by a similar discussion using Equation (4), where the yield stress, σ_Y, is replaced by a critical stress at which multiple dislocations start to move and

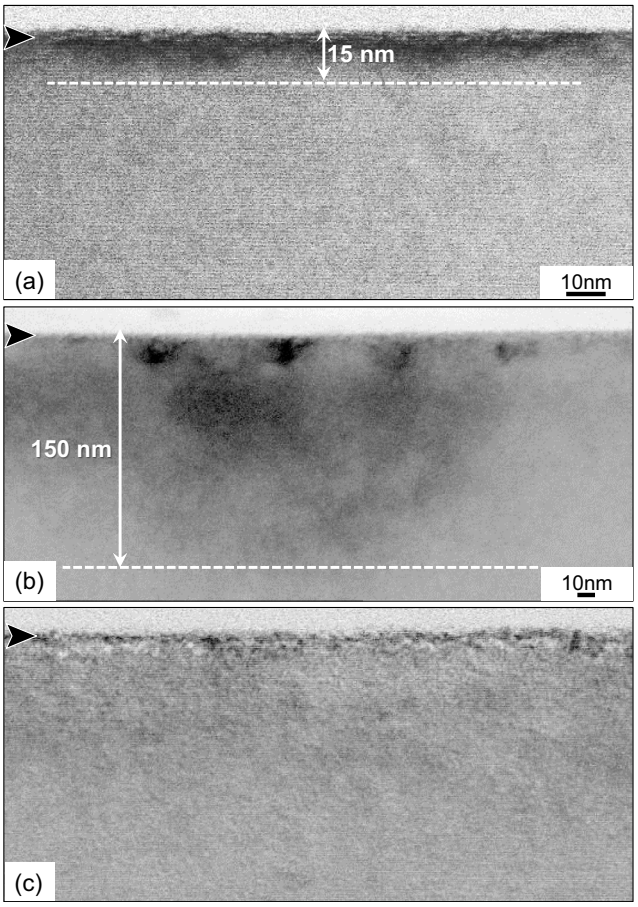

Figure 6. a,b) Magnified views of the top parts indicated by the red frames in Figure 5a and b, respectively. c) STEM image from $[1\bar{1}00]$ direction for the reference (non-loaded) for comparison. ➤ indicates the surface of the specimen.

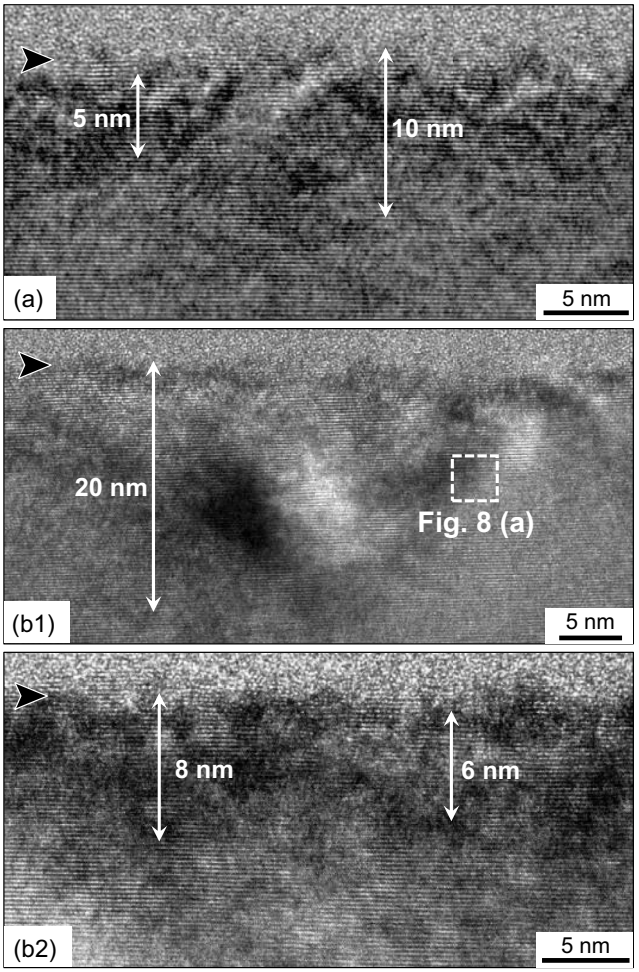

Figure 7. a) and b) (b1,b2) TEM images of the areas of heavily disordered crystal structure with multiple-dislocation pileups observed in Figure 6a,b, respectively. The area border was identified by the lattice distortion. ➤ indicates the surface of the specimen.

accumulate, making the crystal structure disordered. The top surface-neutral plane distance, a, for the specimen A is almost half of that for B, and this depth for the former becomes almost half that for the latter as well, due to the steep stress gradient.

In general, plastic deformation is caused by the accumulation of dislocations, and then, TEM studies were performed for the multiple-dislocation pileups area in the specimen of Figure 7b to investigate the dislocation behaviors. Heavily disordered crystal structures with multiple dislocations were observed in the densest parts, making it difficult to clearly analyze the dislocations. **Figure 8** is one of the TEM observations for the less dense parts of defects; Figure 8a is the magnified view of the part indicated by the white frame in Figure 7b1. For comparison, a TEM lattice image and an electron beam diffraction one from the same direction [1$\bar{1}$00] for the reference (non-loaded) are also given in Figure 8b,c, respectively. The simulation results of Si atoms in 4H-SiC (blue dots) are overlapped with the lattice images in Figure 8a,b. While the simulation coincides with the TEM lattice image in the reference (Figure 8b), some lattice misalignment is confirmed in the (11$\bar{2}$2) plane in Figure 8a. The simulation of Si atoms in the upper left of Figure 8a is obtained by shifting the simulation image of the [1$\bar{1}$00] incidence (lower right) along the (11$\bar{2}$2) plane. A structure consistent with a slip on the (11$\bar{2}$2) plane is confirmed.

The 4H-SiC belongs to the hexagonal crystal system, which has several slip planes including (0001), {10$\bar{1}$0}, {10$\bar{1}$1}, {11$\bar{2}$2}, and {10$\bar{1}$2}.[37–41] It is well known that slip most occurs in parallel with the (0001) plane with the slip direction of <11$\bar{2}$0>.[40] In hexagonal SiC, slip has been reported for the (0001) basal plane/<11$\bar{2}$0> direction (as the most slippery one), the {1$\bar{1}$00} prismatic plane/<11$\bar{2}$0> direction, and the {1$\bar{1}$01} pyramidal plane/<11$\bar{2}$0> direction, etc.[41,42] The previously observed pyramidal slip on the {11$\bar{2}$2} plane has been observed for some hexagonal metals such as Mg, Ti, Zn, and Cd with the <$\bar{1}\,\bar{1}$23> direction[43–45] and has been identified in a simulation study on deformation mechanisms of 6H-SiC.[46] In this study, tensile stress is applied along the <$\bar{1}\,\bar{1}$20> direction, shear stress does not arise on the (0001) plane in principle and thus the basal slip can be excluded from consideration. As previously stated, because of the heavily disordered crystal structures, the clear analyses on the dislocations were difficult in the TEM study. As stated in the introduction, Kishida et al.[18] studied plastic deformation behavior of 6H-SiC single crystals by uniaxial compression using micropillar specimens. When the compression applied in the <$\bar{1}\,\bar{1}$20> direction, which is exactly the same as this study, the clear prismatic slip of {1$\bar{1}$00} plane/<11$\bar{2}$0> direction was almost solely observed with a Schmid factor of 0.433, which is high compared with those of other possible slips when a uniaxial stress applied in this direction. Therefore, it can be considered that this prismatic slip first occurred in this study as well, followed by the occurrence of other slips including the {11$\bar{2}$2}<$\bar{1}\,\bar{1}$23> and {1$\bar{1}$01} <11$\bar{2}$0>, leading to the heavily disordered crystal structures.

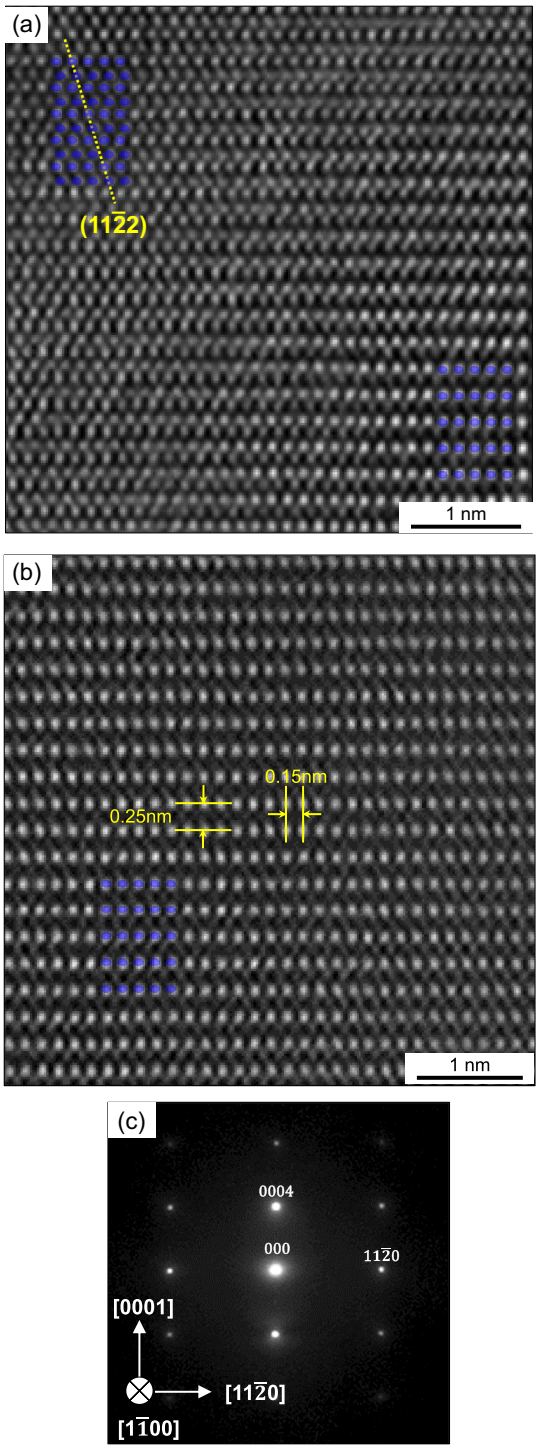

Figure 8. a) Magnified TEM image of the part indicated by the white frame in Figure 7b1. For comparison, b) a TEM lattice image and c) an electron beam diffraction one from [1$\bar{1}$00] direction for the reference (non-loaded).

3.3. CRSS

Slip occurs when the shear stress applied in the slip direction on the slip plane reaches a certain value, so-called CRSS, which can be calculated from the following equation.

$$\tau_{\mathrm{CRSS}} = \sigma m \tag{5}$$

where τ_{CRSS} is the CRSS, σ is the tensile stress, m is the Schmid factor, which is the product of the angle between the slip plane

normal and the tensile direction and that between the slip direction and the tensile direction. Assuming that the first slip occurred on the $\{1\bar{1}00\}$ plane with the $<11\bar{2}0>$ direction as previously discussed, m is 0.433. Substituting the measured yield stresses into σ in Equation (5), the obtained τ_{CRSS} value is the same, 10.9 GPa, for both the specimens *A* and *B* (Table 2).

In the aforementioned study by Kishida et al.[18] the CRSS was also investigated for the $(0001)/<2110>$ basal slip and the $\{1\bar{1}00\}/<11\bar{2}0>$ prismatic one. As stated in the introduction, they found that the CRSS increased with decreasing the specimen size, following an inverse power-law relationship, $\tau_{CRSS} \propto L_E^{\,n}$ (L_E: edge length). For the case of the $\{1\bar{1}00\}/<11\bar{2}0>$ prismatic, the CRSS varied from 6 GPa at $L_E = 5\,\mu m$ to 9 GPa at $L_E = 1\,\mu m$, with $n = 2.1$. Similar size dependence of the yield stress or CRSS has been frequently reported in microscale mechanical testing of metals, including face-centered cubic and body-centered cubic materials. Various models including size-dependent dislocation nucleation[47,48] and dislocation starvation[49] have been proposed to account for this effect, while the source and mechanism have not fully elucidated. Thus, it is difficult to correctly predict the CRSS of this study from the results of Kishida et al.[18] However, the volume subjected to the maximum tensile stress in the microcantilever beam specimens of this study is much smaller than that at $L_E = 1\,\mu m$ in Kishida et al.[18] It is plausible that the CRSS of this study, 10.9 GPa, is higher than theirs, 9 GPa, due to this volume effect. In addition, Pizzagalli[19] theoretically estimated Peierls stresses for basal and prism plane slip systems of 2H-, 4H-, and 3C-SiC single crystals using first-principles calculations. The calculated stress for the prism-plane slip of 4H-SiC was 10.1 GPa, which shows a good agreement with the CRSS of this study, 10.9 GPa. Therefore, this value is reasonable for the CRSS of the 4H-SiC $\{1\bar{1}00\}/<11\bar{2}0>$ prismatic slip. In other words, the CRSS values for *A* and *B* are the same, most likely because they both have reached the theoretical one (or the stress without influence of crystallographic defects) due to the very limited area which is subjected to the maximum tensile stress.

3.4. Fracture Strength

The fracture strength, σ_f, which was calculated by using Equation (1), was 41.9 ± 2.8 and 33.5 ± 2.4 GPa for the specimens *A* and *B*, respectively (Table 2). Again, since all the fractures occurred in the nonlinearity range, the calculated values lack entire rigorousness. Using first-principles density functional theory calculations, etc., Umeno et al.[50] and Kubo et al.[51] investigated ideal tensile strength of various polytype structures of SiC; in terms of 4H-SiC, the ideal tensile strength in the $<11\bar{2}0>$ direction, which was reached after significant yielding phenomenon or plastic deformation, was estimated to be 47–55 GPa. The fracture strength obtained for *A*, 41.9 GPa, is relatively close to this ideal strength.

According to the linear fracture mechanics, σ_f, can be related to the crack size of the fracture origin through the fracture toughness, K_{IC}, which is expressed by the following equation.

$$\sigma_f = \frac{K_{IC}}{Y\sqrt{\pi c}} \tag{6}$$

where Y is the crack shape factor and c is the crack length. Assuming two types of crack, a Griffith crack and a penny-shaped one, $Y = 1$ and $2/\pi$, respectively. Kunka et al.[52] carefully investigated K_{IC}. values for $\{01\bar{1}0\}$ and $\{11\bar{2}0\}$ planes of 4H- and 6H-SiC single crystals by using Knoop indentations, resulting in 1.4 and 1.8 MPa $m^{1/2}$ for 4H and 1.5 and 1.9 MPa $m^{1/2}$ for 6H, respectively. Kishida et al.[18] also studied fracture toughness for 6H-SiC single crystals by using a chevron-notched beam test which is one of the most reliable K_{IC} measurement methods. They estimated the K_{IC} values to be 1.37 ± 0.13 and 1.57 ± 0.13 MPa $m^{1/2}$ for specimens with a notch plane being parallel to the (0001) and $\{01\bar{1}0\}$ planes, respectively. Although Kishida et al. did not measure those for a $\{11\bar{2}0\}$ plane, there is a good agreement between these two studies for the K_{IC} value of the 6H $\{01\bar{1}0\}$ plane. Thus, we employ 1.8 MPa $m^{1/2}$ for the K_{IC} value in Equation (6), from the results of Kunka et al. The equivalent crack sizes, $2c$, calculated for a Griffith crack and a penny-shaped one are 1.2 and 2.9 nm for the specimen *A* and 1.8 and 4.5 nm for *B*, respectively (Table 2). It should be noted, however, that the estimated crack size is so small that it is uncertain whether they meet strictly criteria of small scale yielding of linear fracture mechanics, allowing only a relative comparison. Fractographic study was conducted for the fracture surfaces of the specimens *A* and *B* using SEM; however, the fracture origins were not clearly identified because of such small defect sizes. **Figure 9** shows an SEM image of a fracture surface of the specimen *B* as an example. It is observed that the fracture crack tends to proceed along the cleavage planes of (0001).

It is known that dislocations are involved both in the initiation and propagation of cracks and that dislocation pileups tend to cause stress concentration and/or crack formation, which possibly act as fracture origins of materials.[20–22] Stress concentration occurs at a crack tip, and such stress field is also represented by a dislocation array.[20,21] Although the distribution of edge

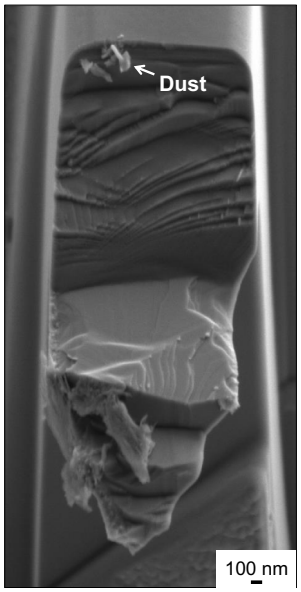

Figure 9. SEM image of fracture surface after a bending test for the specimen *B*. Dusts identified as carbon by X-ray photoelectron spectroscopy are attached to the upper side of the specimen *B*.

dislocations equivalent to mode I crack cannot form by plastic deformation caused by dislocation slip, that equivalent to mode II crack is possible to occur by the dislocation pileups moving on a slip plane (when it meet some obstacles).[20] In addition, it is generally known that one typical source of cracks is the interaction of different slips, causing dislocation pileups and cleavage cracks generated at the intersections of two different slip planes.[20,22] For example, Fang et al.[22] demonstrated dislocation-based crack initiation and propagation in single-crystal $SrTiO_3$; a locally stressed volume at small scale undergoes dislocation on primary slip planes that are 45° inclined to the surface and then dislocation on secondary slip planes perpendicular to the surface, followed by crack initiation and propagation due to dislocation pileups, etc.

The areas of heavily disordered crystal structures with multiple-dislocation pileups were observed in Figure 7a,b; the area depth was 5–10 and 6–20 nm for the specimens *A* and *B*, respectively, due to the steeper stress gradient of *A*. It should be noted that the estimated equivalent crack size, 2*c*, is smaller than the area depth for each of *A* and *B*, and that the ratio between the two values (crack size and area depth) is almost equal. Thus, it is reasonable to think that cracks form within this multiple-dislocation pileup area, by the above stated interaction with dislocation pileups. The cracks formed in this fashion can act as the fracture origins. The larger area of multiple-dislocation pileups is likely to lead to the greater crack formation, resulting in the lower fracture strength of *B*.

As already mentioned, the specimen *A* showed the very high fracture strength of 41.9 GPa, which is close to the ideal tensile strength of 4H-SiC in the $<11\bar{2}0>$ direction, 47–55 GPa.[50,51] Most presumably, this high strength is possible because of the seep stress gradient of the specimen *A*, which substantially restricts the expansion of the multiple dislocation pileup area and suppress the resultant crack formation. It is worthy of noting, however, that Tatami et al.[27] investigated grain boundary strength of silicon carbide bicrystals using microcantilever bending tests (the same as this study) and found that the strength was distributed from 19 to 62 GPa, indicating that a very high strength was possible depending on the crystal orientations of the two adjacent grains. In addition, the first-principles density functional theory calculations revealed that the ideal tensile strength of 3C-SiC ranged, depending on the crystal orientation, from ≈45 GPa in <111> direction and ≈50 GPa in <110> to as high as ≈90 GPa in <100>.[50] Thus, there is a possibility that a tensile strength higher than those measured in this study exists for SiC single crystals.

4. Conclusions

In this study, we evaluated the deformation behaviors and mechanical properties of 4H-SiC single crystals using microcantilever beam specimens with two different sizes, *A* and *B* ($A < B$). The tensile stress was applied along $<\bar{1}\,\bar{1}20>$ direction. The plastic deformation, or nonlinearity, was observed in the stress–strain curves, and the stress at the proportional limit was defined as the yield stress, which coincided between the two specimens at $\approx 25 \pm 2$ GPa. The STEM and TEM studies indicated that the plastic deformation was due to the dislocation activities. The multiple-dislocation pileup areas were observed in both the specimens, but the depth of the area of *A* (5–10 nm) was almost half of that of *B* (6–20 nm), due to the steeper stress gradient. Assuming the $\{1\bar{1}00\}/<11\bar{2}0>$ prismatic slip which most plausibly occurs in the $<\bar{1}\,\bar{1}20>$ stress application, the CRSS was estimated to be 10.9 GPa, which agreed well with the previous studies. Despite the identical yield stresses, the measured fracture strength was 41.9 ± 2.8 and 33.5 ± 2.4 GPa for the specimens *A* and *B*, respectively. The relationship between the fracture and the dislocations was discussed on the basis of dislocation-based fracture mechanics and others. It was suggested that cracks form within the above multiple-dislocation pileup area, by the interaction with the dislocation pileups and act as the fracture origins. The larger area of multiple-dislocation pileups is likely to lead to the greater crack formation, resulting in the fracture strength difference. The strength of the specimen *A* was close to the ideal tensile strength of 4H-SiC in the $<11\bar{2}0>$ direction, 47–55 GPa, estimated by the first-principles density functional theory calculations, etc.

Supporting Information

Supporting Information is available from the Wiley Online Library or from the author.

Acknowledgements

This work was supported by JST, CREST grant No. JPMJCR2192, Japan.

Conflict of Interest

The authors declare no conflict of interest.

Data Availability Statement

The data that support the findings of this study are available on request from the corresponding author. The data are not publicly available due to privacy or ethical restrictions.

Keywords

critical resolved shear stresses, deformations, dislocations, silicon carbides, single crystals, strengths

Received: January 15, 2024
Revised: February 21, 2024
Published online:

[1] Y. Katoh, L. L. Snead, C. H. Henager, T. Nozawa, T. Hinoki, A. Iveković, S. Novak, S. M. Gonzalez de Vicente, *J. Nucl. Mater.* **2014**, *455*, 387.
[2] H. Tanaka, *J. Ceram. Soc. Jpn.* **2011**, *119*, 218.
[3] X. W. Yin, L. F. Cheng, L. T. Zhang, N. Travitzky, P. Greil, *Int. Mater. Rev.* **2017**, *62*, 117.
[4] S. Fan, Y. Du, L. He, C. Yang, H. Liu, L. F. Cheng, L. T. Zhang, N. Travitzky, *Tribol. Int.* **2016**, *102*, 10.

[5] D. Galsterer, N. Travitzky, T. Wolff, P. Greil, *Adv. Eng. Mater.* **2008**, *10*, 1134.
[6] D. Hotza, M. Di Luccio, M. Wilhelm, Y. Iwamoto, S. Bernard, J. C. Diniz da Costa, *J. Membr. Sci.* **2020**, *610*, 118193.
[7] L. Schlier, W. Zhang, N. Travitzky, P. Greil, J. Cypris, M. Weclas, *Int. J. Appl. Ceram. Technol.* **2011**, *8*, 1237.
[8] R. Falgenhauer, P. Rambacher, L. Schlier, J. Volkert, N. Travitzky, P. Greil, M. Weclas, *Appl. Therm. Eng.* **2017**, *112*, 1557.
[9] R. Powell, L. B. Rowland, *Proc. IEEE* **2002**, *90*, 942.
[10] F. Jiang, Y. Liu, Y. Yang, Z.-R. Huang, D. Li, G.-L. Liu, X.-J. Liu, *J. Nanomater.* **2012**, *2012*, 984048.
[11] C. R. Eddy, D. K. Gaskill, *Science* **2009**, *324*, 1398
[12] X. She, A. Q. Huang, Ó. Lucía, B. Ozpineci, *IEEE Trans. Ind. Electron.* **2017**, *64*, 8193.
[13] N. W. Jepps, T. F. Page, *Prog. Cryst. Growth Charact. Mater.* **1983**, *7*, 259.
[14] C. Shin, H. H. Jin, W.-J. Kim, J.-Y. Park, *J. Am. Ceram. Soc.* **2012**, *95*, 2944.
[15] S. Kiani, K. W. K. Leung, V. Radmilovic, A. M. Minor, J.-M. Yang, D. H. Warner, S. Kodambaka, *Acta Mater.* **2014**, *80*, 400.
[16] B. Chen, J. Wang, Y. Zhu, X. Liao, C. Lu, Y.-W. Mai, S. P. Ringer, F. Ke, Y. Shen, *Acta Mater.* **2014**, *80*, 392.
[17] G. Kwon, H.-H. Jo, S. Lim, C. Shin, H.-H. Jin, J. Kwon, G.-M. Sun, *J. Mater. Sci.* **2015**, *50*, 8104.
[18] K. Kishida, Y. Shinkai, H. Inui, *Acta Mater.* **2020**, *187*, 19.
[19] L. Pizzagalli, *Acta Mater.* **2014**, *78*, 236.
[20] J. Weertman, *Dislocation Based Fracture Mechanics*, World Scientific Publishing, Singapore **1996**.
[21] C. S. Pande, R. Goswami, *Metals* **2020**, *10*, 473.
[22] X. Fang, K. Ding, C. Minnert, A. Nakamura, K. Durst, *J. Mater. Sci.* **2021**, *56*, 5479.
[23] E. Camposilvan, O. Torrents, M. Anglada, *Acta Mater.* **2014**, *80*, 239.
[24] J. Tatami, M. Katayama, M. Ohnishi, T. Yahagi, T. Takahashi, T. Horiuchi, M. Yokouchi, K. Yasuda, D. K. Kim, T. Wakihara, K. Komeya, *J. Am. Ceram. Soc.* **2015**, *98*, 965.
[25] A. D. Norton, S. Falco, N. Young, J. Severs, R. I. Todd, *J. Eur. Ceram. Soc.* **2015**, *35*, 4521.
[26] R. Henry, T. Blay, T. Douillard, A. Descamps-Mandine, I. Zacharie-Aubrun, J.-M. Gatt, C. Langlois, S. Meille, *Mech. Mater.* **2019**, *136*, 103086.
[27] J. Tatami, Y. Imoto, T. Yahagi, T. Takahashi, M. Iijima, *J. Eur. Ceram. Soc.* **2020**, *40*, 2634.
[28] H. Yamaguchi, J. Tatami, T. Yahagi, H. Nakano, M. Iijima, T. Takahashi, T. Kondo, *J. Mater. Sci.* **2020**, *55*, 7359.
[29] T. Csanádi, M. Vojtko, Z. Dankházi, M. J. Reece, J. Dusza, *J. Eur. Ceram. Soc.* **2020**, *40*, 4774.
[30] T. Csanádi, M. Gall, M. Vojtko, A. Kovalčíková, M. Hnatko, J. Dusza, P. Šajgalík, *J. Eur. Ceram. Soc.* **2020**, *40*, 4783.
[31] T. Csanádia, M. Vojtkoa, J. Duszaa, *Int. J. Refract. Met. Hard Mater.* **2020**, *87*, 105163.
[32] M. Tanabe, J. Tatami, M. Iijima, T. Yahagi, T. Takahashi, H. Nakano, T. Ohji, *J. Am. Ceram. Soc.* **2023**, *106*, 5431.
[33] M. Muramoto, J. Tatami, M. Iijima, K. Matsui, T. Yahagi, T. Takahashi, H. Nakano, T. Ohji, *J. Eur. Ceram. Soc.* **2024**, *44*, 1061.
[34] T. Csanádi, A. Azizpour, M. Vojtko, W. G. Fahrenholtz, *J. Am. Ceram. Soc.* **2024**, *107*, 1669.
[35] Y. Seto, M. Ohtsuka, *J. Appl. Cryst.* **2022**, *55*, 397.
[36] H. Kitahara, Y. Noda, F. Yoshida, H. Nakashima, N. Shinohara, H. Abe, *J. Ceram. Soc. Japan* **2001**, *109*, 602.
[37] H. Fan, J. A. El-Awady, *J. Appl. Mech.* **2015**, *82*, 101006.
[38] Z. Zheng, D. S. Balint, F. P. E. Dunne, *Acta Mater.* **2016**, *107*, 17.
[39] S.-G. Hong, S. H. Park, C. S. Lee, *Acta Mater.* **2010**, *58*, 5873.
[40] T. B. Britton, F. P. E. Dunne, A. J. Wilkinson, *Proc. R. Soc. A* **2015**, *471*, 20140881.
[41] K. Maeda, K. Suzuki, S. Fujita, M. Ichihara, S. Hyodo, *Philos. Mag. A* **1988**, *57*, 573.
[42] S. Amelinckx, G. Strumane, W. W. Webb, *J. Appl. Phys.* **1960**, *31*, 1359.
[43] T. Obara, H. Yoshinga, S. Morozumi, *Acta Metall.* **1973**, *21*, 845.
[44] Y. Minonishi, S. Morozumi, H. Yoshinaga, *Scr. Metall.* **1982**, *16*, 427.
[45] H. Tonda, S. Ando, *Metall. Mater. Trans. A* **2002**, *33*, 831.
[46] Z. Wu, W. Liu, L. Zhang, *Comput. Mater. Sci.* **2017**, *137*, 282.
[47] T. A. Parthasarathy, S. I. Rao, D. M. Dimiduk, M. D. Uchic, D. R. Trinkle, *Scr. Mater.* **2007**, *56*, 313.
[48] S. I. Rao, D. M. Dimiduk, M. Tang, M. D. Uchic, T. A. Parthasarathy, C. Woodward, *Philos. Mag.* **2007**, *87*, 4777.
[49] J. R. Greer, W. D. Nix, *Phys. Rev. B.* **2006**, *73*, 245410.
[50] Y. Umeno, A. Kubo, S. Nagao, *Comput. Mater. Sci.* **2015**, *109*, 105.
[51] A. Kubo, S. Nagao, Y. Umeno, *Comput. Mater. Sci.* **2017**, *139*, 89.
[52] C. Kunka, A. Trachet, G. Subhash, *J. Am. Ceram. Soc.* **2015**, *98*, 1891.